Periodicity Search on X-Ray Bursts of SGR J1935+2154 Using 8.5 yr of Fermi/GBM Data

Jin-Hang Zou[1,2] , Bin-Bin Zhang[2,3,4] , Guo-Qiang Zhang[2,3] , Yu-Han Yang[2,3] , Lang Shao[1] , and Fa-Yin Wang[2,3]
[1] College of Physics, Hebei Normal University, Shijiazhuang 050024, People's Republic of China; lshao@hebtu.edu.cn
[2] School of Astronomy and Space Science, Nanjing University, Nanjing 210093, People's Republic of China; bbzhang@nju.edu.cn
[3] Key Laboratory of Modern Astronomy and Astrophysics (Nanjing University), Ministry of Education, People's Republic of China
[4] Department of Physics and Astronomy, University of Nevada Las Vegas, NV 89154, USA

Abstract

We performed a systematic search for X-ray bursts of the SGR J1935+2154 using the Fermi Gamma-ray Burst Monitor continuous data dated from 2013 January to 2021 October. Eight bursting phases, which consist of a total of 353 individual bursts, are identified. We further analyze the periodic properties of our sample using the Lomb–Scargle periodogram. The result suggests that those bursts exhibit a period of ~238 days with a ~63.2% duty cycle. Based on our analysis, we further predict two upcoming active windows of the X-ray bursts. Since 2021 July, the beginning date of our first prediction has been confirmed by the ongoing X-ray activities of the SGR J1935+2154.

Unified Astronomy Thesaurus concepts: Radio transient sources (2008); Soft gamma-ray repeaters (1471)

1. Introduction

Soft gamma-ray repeaters (SGRs), the X-ray/gamma-ray transient sources that exhibit explosive activity about every year or decade, are known to be magnetars (van Kerkwijk et al. 1995; Banas et al. 1997; Fuchs et al. 1999; Vrba et al. 2000), the young neutron stars with strong magnetic fields (Duncan & Thompson 1992; Paczynski 1992; Thompson & Duncan 1995, 1996; Kouveliotou et al. 1998b). Such a magnetar origin of the SGRs has been confirmed by a few recent cases such as SGR 1806-20 (Mazets & Golenetskii 1981), SGR 0526-66 (Mazets et al. 1979c, 1979b), SGR 1627-14 (Kouveliotou et al. 1998a; Woods et al. 1999), SGR 1900+14 (Mazets et al. 1979a; Kouveliotou et al. 1993), and SGR J1935+2154 (Stamatikos et al. 2014), all of which are listed in the magnetar catalog[5] (Olausen & Kaspi 2014) without any counterexample.

According to their brightness, the SGR bursts can be roughly divided into three classes (Woods & Thompson 2006):

1. Short-duration bursts: the most common type of bursts with typical duration of about 0.1 s and spectra characterized by the Optically Thin Thermal Bremsstrahlung model.

2. Giant flares (GFs): unusual intense bursts with energy about a thousand times higher than that of a typical burst, characterized by an initial hard initial spike and the rapidly decaying tails with pulsations (e.g., Mazets et al. 1979b; Hurley et al. 1999). Some short gamma-ray bursts (GRBs), namely, GRB 051103 (Ofek et al. 2006; Frederiks et al. 2007), GRB 070201 (Mazets et al. 2008; Ofek et al. 2008), GRB 200415A (Yang et al. 2020; Svinkin et al. 2021), and a few more, are indeed found to be magnetar-giant-flare originated (Burns et al. 2021).

3. Intermediate bursts (IBs): intermediate bursts with peak flux, duration, and energy between the short-duration bursts and GFs (e.g., Golenetskii et al. 1984; Guidorzi et al. 2004). They tend to have abrupt onsets as well as abrupt endpoints (Woods & Thompson 2006) if the duration is less than the rotation period (~a few seconds) of the magnetar.

Multiwavelength afterglows are observed in both IBs and GFs. For example, a radio afterglow event (Cameron et al. 2005) has been observed from SGR 1806-20 after its GF in 2005 January (Boggs et al. 2005). Two X-ray afterglow events have been observed from SGR 1900+14, followed by its GF in 1998 August and IB in 2001 April, respectively (Woods et al. 2001; Feroci et al. 2003), and a radio afterglow has been observed following the GF of the same SGR in 1998 August (Frail et al. 1999).

SGR J1935+2154 is a Galactic magnetar, which was first observed by the Swift Burst Alert Telescope (BAT) in 2014 (Stamatikos et al. 2014). It has experienced four active windows before 2020, respectively, in 2014, 2015, 2016, and 2019 (Younes et al. 2017; Lin et al. 2020a). 2020 April was recognized as the most violent bursting month of SGR J1935+2154 so far, during which a burst forest was observed. These bursts consist of the first X-ray counterpart (Li et al. 2021; Mereghetti et al. 2020; Tavani et al. 2020; Ridnaia et al. 2021) that is associated with a fast radio burst, FRB 200428 (Bochenek et al. 2020; CHIME/FRB Collaboration et al. 2020a).

FRBs are millisecond radio transients with large dispersion measures (DMs ~100–2600 pc cm^{-3}; Lorimer et al. 2007; Cordes & Chatterjee 2019; Petroff et al. 2019; Xiao et al. 2020; Zhang 2020). Although hundreds of FRBs have been observed so far,[6] the physical models are still under debate (for a recent review, see Platts et al. 2019). Multiple models suggest that

---

[5] http://www.physics.mcgill.ca/~pulsar/magnetar/main.html

[6] http://frbcat.org/

FRBs can originate from a magnetar. Those models involve giant flares of a magnetar, the interactions between magnetar flares and their surroundings (Kulkarni et al. 2014; Lyubarsky 2014; Katz 2016; Beloborodov 2017; Metzger et al. 2017), and the collision of a magnetar and an asteroid (Geng & Huang 2015; Dai et al. 2016). Interestingly, the statistical properties of FRBs are similar as those of Galactic magnetar bursts (Wang & Yu 2017; Wadiasingh & Timokhin 2019; Cheng et al. 2020). The association between an X-ray burst of SGR J1935+2154 and FRB 200428 supports that at least some FRBs are produced by magnetars (CHIME/FRB Collaboration et al. 2020a; Bochenek et al. 2020).

The magnetar association of FRBs motivated us to search for the common properties shared by the two phenomena. An interesting manner of repeating FRBs is the periodic window behavior (PWB), proposed in the bursts of FRB 121102 and FRB 180916. The PWB describes a quasi-periodic phenomenon that bursting phases always appear periodically, but there is no periodicity for specific bursts. CHIME/FRB Collaboration et al. (2020b) first reported a possible period about 16.35 days for FRB 180916. They collected 38 bursts that occurred from 2018 September to 2020 February and located these bursts in a 5 day phase window. Rajwade et al. (2020) suggested a possible PWB of about 160 days for FRB 121102. This result was also confirmed by Cruces et al. (2021). Many models have been proposed to explain those periods, including those involved with the precession of magnetars (Levin et al. 2020; Zanazzi & Lai 2020), the orbit motion of binary stars (Ioka & Zhang 2020; Lyutikov et al. 2020), the ultra-long period magnetars (Beniamini et al. 2020), the luminous X-ray binaries (Sridhar et al. 2021) and the magnetar-asteroid model (Dai & Zhong 2020).

PWBs have also been investigated for SGRs. Zhang et al. (2021) analyzed the bursts of SGR 1806-20, and estimated a possible period of about 395 days. Grossan (2021) suggested a possible PWB with a period of about 231 days for SGR J1935+2154 using the observations from IPN[7] (Interplanetary Network) instruments. The PWB was further studied by Denissenya et al. (2021) using the likelihood analysis.

In this Letter, We performed a systematic search for X-ray bursts of the SGR J1935+2154 using the Fermi Gamma-ray Burst Monitor (GBM; Meegan et al. 2009) continuous data dated from 2013 January to 2021 July, aiming to identify its PWB using an unbiased sample. In Section 2, we describe the search procedure and report the results of our search. In Section 3, we use the Lomb–Scargle method to analyze the results and show that SGR J1935+2154 has a bursting period of about 238 days. Finally, brief implications and discussions are provided in Section 4.

2. Burst Search

Due to the limit of detector sensitivity, not all SGR bursts can trigger Fermi/GBM. Therefore, an untriggered search is needed to identify all potential bursts throughout the available data (Lin et al. 2020a). Many searches have been carried out (e.g., Lin et al. 2020b, 2020c; Mereghetti et al. 2020; Younes et al. 2020; Yang et al. 2021). We independently searched the continuous time-tagged event (CTTE) data of Fermi/GBM Na I detectors within the range of 8–900 keV from 2013-01-01T00:00:00 (UTC) to 2021-10-21T23:59:59 (UTC), including

the latest explosive activity of SGR J1935+2154 in July by the following three steps:

1. *Data reduction and burst window selection.*

    The first step is to determine the data search windows in CTTE data that exclude the South Atlantic Anomaly (SAA) and contains possible bursts. The SAA passage can be easily determined by calculating the Fermi's longitude and latitude through the position history files released on Fermi/GBM data.[8] To further determine the searching window, we first downloaded the hourly separated CTTE data of 12 sodium iodide (Na I) scintillators on board Fermi/GBM, binned them into 40 ms bin size, and obtained the corresponding light curves.[9] The time ranges with zero count rate (e.g., due to the SAA passage) are excluded. The hourly data may be cut into one more pieces due to the SAA passage or missing data. Then, for each continuous piece, we constructed a background model using the baseline method implemented in R language.[10] Based on the modeled background, we can further select the qualified background range using the sigma clipping method,[11] within which the observed count rates are consistent with the background level. Based on the Gaussian fit of the count rate within the background range, we can further determine the 3σ confidence level of the background. Finally, the burst search windows can be determined by bracketing the regions where $C_{\mathrm{obs},i} - B_i \geqslant 3\sigma$, which are used in step 2 below.

2. *Burst identification by the Bayesian block method.*

    In this step, we apply the Bayesian blocks method (Scargle et al. 2013) to the burst windows found in Step 1 and identify burst candidates based on their temporal properties. The Bayesian blocks (BB) method[12] is a nonparametric modeling technique for detecting and characterizing local variability in time-series data (Scargle et al. 2013). It maximizes the likelihood to find the best segmentation or boundary between blocks, called the "change point," and has been used in untriggered searches in some previous studies (e.g., Lin et al. 2020a, 2020b, 2020c; Yang et al. 2021).

    For each burst window, we exact the light curves of 12 Na I detectors. Each light curve is ensured to cover at least three times the window width. We used the change points obtained by the BB method to divide it into "blocks." Each of those blocks, by definition, can be characterized as having a constant block rate ("block rate"), which can be calculated by averaging the rate within the block. The longest block, which is also automatically the lowest one, provides us the first "background block" to measure the background level. Ordered by their lengths, two to four additional blocks are checked and selected as background blocks if their block rates are consistent at the 1σ level with that of the
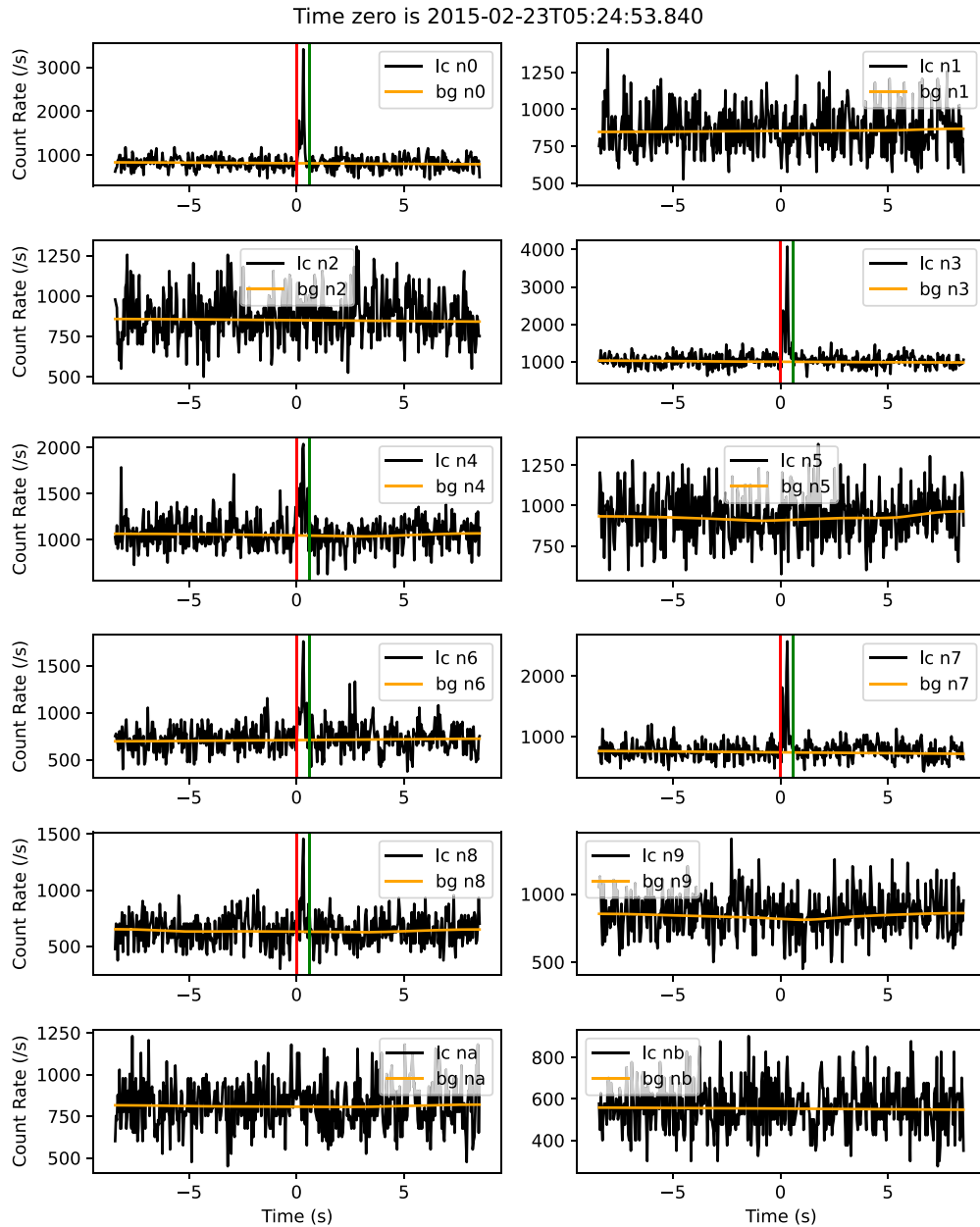

Figure 1. An example of a short-duration burst in our sample. The black curves represent the light curves (lc) of 12 Na I detectors, and the orange lines represent the background (bg) of each light curve. The red lines and the green lines represent the starting time and the ending time of the burst recorded in each detector, respectively. The starting time of this burst is 2015-02-23T05:24:53.840 (UTC).

longest one. The final background region contains 2–5 background blocks.

Next, an array of Boolean values is assigned with "True" for the light-curve data within the background region, and "False" otherwise. The background level of the whole burst window can then be calculated using the Whittaker Smoother method (Whittaker 1922; Eilers 2003).

Finally, the background level can be used to calculate the significance, S, of each block according to Equation (15) in Vianello (2018). If S exceeds the threshold, 3, the block is recorded as a burst block candidate. We require that a qualified burst block must present in at least two Na I detectors. Eventually, all the burst blocks form a "burst" candidate, and the spreading length of the burst blocks defines the burst duration. By

requiring $S > 3$, more than 1000 burst candidates are generated in this step. An example of our burst candidates is shown in Figure 1.

3. *Burst confirmation by localization.*

The burst candidates are then localized and checked if they consistently conform with the location of SGR J1935+2154 at the 1σ level. We developed our own localization code following the method in Connaughton et al. (2015) and Burgess et al. (2018). By employing the response matrix generator *gbm_drm_gem*[13] and the related database, our code can calculate the expected modeled count rate ratios among 12 Na I detectors for any directions. The burst location can be determined by maximizing the likelihood ratio between the modeled and

---

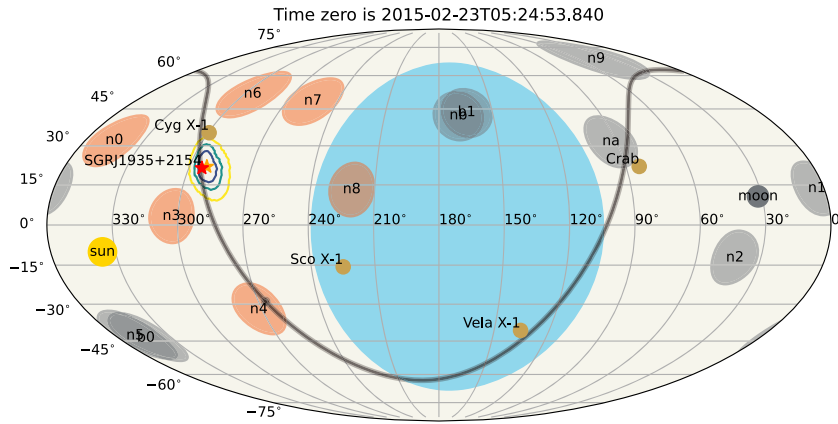[13] https://github.com/grburgess/gbm_drm_gen

Figure 2. The localization of the same burst in Figure 1. The small circles represent the pointing directions of Na I detectors, which can be calculated from the satellite attitude data available in the Fermi/GBM data products. The detectors illuminated and nonilluminated by SGR J1935+2154 are filled with orange and gray colors, respectively. The red star indicates SGR J1935+2154, and the yellow star indicates the location calculated by our code. The three contour lines in different colors represent the 1σ, 2σ, and 3σ credible regions, respectively. The brown dots mark the locations of four bright X-ray sources, namely Cygnus X-1, Sco X-1, Vela X-1, and Crab. The black curve represents the projection of the galactic plane. The blue area represents the sky region occulted by the Earth.

observed data. An example of our localization results is shown in Figure 2. To verify the validation of our localization method, we selected the recent 121 confirmed bursts in previous studies (Lin et al. 2020a, 2020c; Younes et al. 2020) and plot our location results for them in Figure 3(a). We found that the 1σ distance between the SGR and our locations is an adequate one to claim the association between our bursts and the SGR 1935+2154. The averaged 1σ uncertainties of this subsample is $8°.39$. In addition, we plotted the locations of all the bursts in our sample in Figure 3 (b) and found the 1σ measurement could also apply to other bursts. In particular, the averaged 1σ value of the whole sample is $9°.15$, which is consistent with the previous subsample.

We obtained 356 burst candidates after the above three steps. Those candidates were further screened manually to ensure no previous study had claimed they were from other nearby sources. We found that more than 65% of the candidates in our sample have been previously studied or collected in the literature (e.g., Lin et al. 2020a, 2020b, 2020c) and various resources (such as the IPN SGR Burst list[14]) as bursts of SGR J1935+2154, which confirms our results. On the other hand, a burst found at 2019-11-14T19:50:42 was excluded according to the IPN SGR Burst list, which considered the burst as one from SGR 1900+14. In addition, two GRBs (GRB 190619B and GRB 201218A) were also excluded after cross-checking the Fermi GBM GRB catalog.[15] We finally obtained 353 bursts in our sample, which, based on our analysis, are associated with SGR J1935+2154.

All the bursts of our results are listed in Table 1, and highlighted via their burst rate (with a bin size of one day) in the timeline in Figure 4. We note that there are eight bursting phases, starting from 2014 July, 2015 February, 2016 May, 2019 October, 2020 April, 2021 February, and 2021 June, respectively. We also emphasize that there was no burst found in our search in 2017 and 2018, although the sky coverage of Fermi/GBM data was as usual.

Most bursts of our sample are short-duration bursts (see Figure 1 for an example). A burst forest was observed on 2020
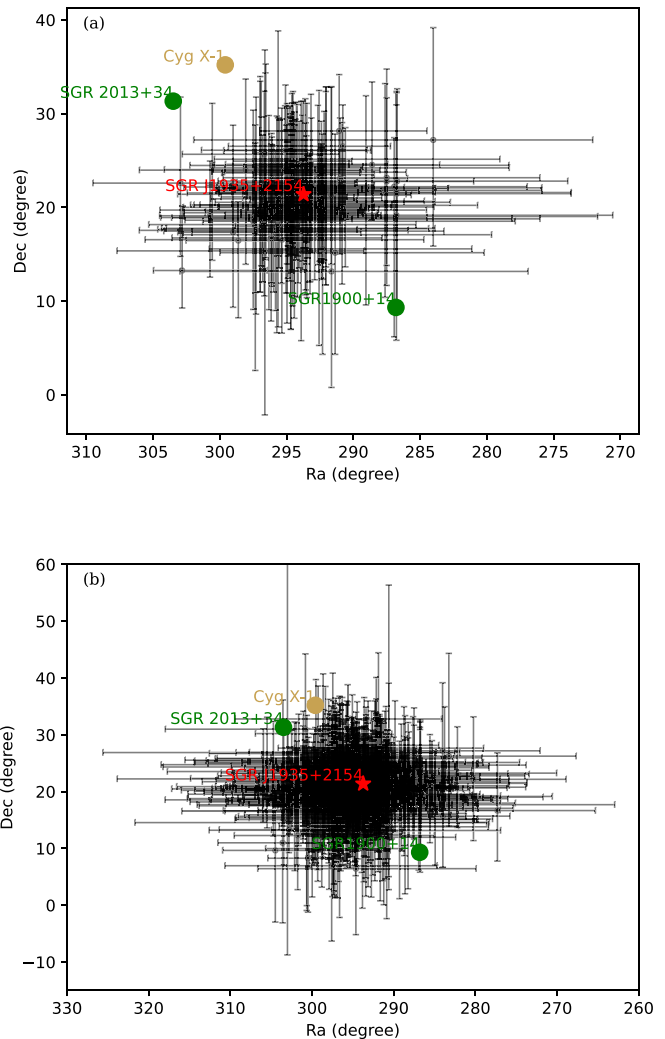
Figure 3. The top panel (a) shows the localization of 121 confirmed bursts of SGR J1935+2154 observed by Fermi/GBM. The red star represents the coordinates of SGR J1935+2154. The two green points are SGR 2013+34 and SGR 1900+14. The brown point is Cygnus X-1. Black dots and lines represent our localization and 1σ localization error. The bottom panel (b) shows the localization of all the bursts in our sample.

Table 1
The Sample of the X-Ray Bursts of SGR J1935+2154

Burst Time (UTC)	Duration (s) 8-900 keV	Burst Time (UTC)	Duration (s) 8-900 keV	Burst Time (UTC)	Duration (s) 8-900 keV
2014-07-05T09:32:48.640	0.12	2016-06-30T10:02:26.000	0.08	2020-04-27T18:35:57.640	0.04
2014-07-05T09:37:34.480	0.04	2016-07-04T14:33:38.640	0.12	2020-04-27T18:36:45.400	1.00
2014-12-27T02:16:21.280	0.12	2016-07-09T16:54:28.200	0.32	2020-04-27T18:38:20.200	0.16
2015-02-22T13:33:00.000	0.12	2016-07-15T07:09:11.720	0.08	2020-04-27T18:38:53.720	0.24
2015-02-22T14:33:20.240	0.28	2016-07-18T09:36:06.520	0.12	2020-04-27T18:40:15.040	0.48
2015-02-22T17:57:05.960	0.08	2016-07-18T09:36:07.120	0.08	2020-04-27T18:40:32.280	0.40
2015-02-22T19:24:45.960	0.04	2016-07-21T09:36:13.680	0.20	2020-04-27T18:40:33.120	0.40
2015-02-22T19:44:16.880	0.08	2016-08-25T07:26:53.480	0.44	2020-04-27T18:42:40.800	0.08
2015-02-22T19:58:16.640	0.16	2016-08-26T14:05:52.920	0.16	2020-04-27T18:42:50.680	0.32
2015-02-22T23:57:33.880	0.12	2019-10-04T09:00:53.600	0.12	2020-04-27T18:44:04.640	0.72
2015-02-23T01:38:07.960	0.08	2019-11-04T01:20:24.000	0.20	2020-04-27T18:46:08.760	0.24
2015-02-23T05:05:06.520	0.08	2019-11-04T02:53:31.360	0.08	2020-04-27T18:46:39.440	0.04
2015-02-23T05:24:53.840	0.52	2019-11-04T04:26:55.880	0.08	2020-04-27T18:46:40.160	0.28
2015-02-23T06:45:40.080	0.08	2019-11-04T07:20:33.720	0.12	2020-04-27T18:46:40.760	0.32
2015-02-23T14:26:16.240	0.08	2019-11-04T09:17:53.480	0.64	2020-04-27T18:47:05.760	0.12
2015-02-23T16:13:52.480	0.04	2019-11-04T10:44:26.280	0.20	2020-04-27T18:48:38.680	0.08
2015-02-24T06:48:47.160	0.08	2019-11-04T12:38:38.520	0.16	2020-04-27T18:49:28.040	0.64
2015-02-25T10:51:03.600	0.12	2019-11-04T15:36:47.440	0.40	2020-04-27T19:36:05.120	0.04
2015-02-28T10:56:48.800	0.08	2019-11-04T20:13:42.560	0.04	2020-04-27T19:37:39.320	0.76
2015-03-01T07:28:54.120	0.08	2019-11-04T20:29:39.760	0.32	2020-04-27T19:43:44.560	0.52
2015-05-15T18:16:51.280	0.16	2019-11-04T23:16:49.560	0.08	2020-04-27T19:45:00.480	0.12
2015-12-06T23:49:57.240	0.04	2019-11-04T23:48:01.360	0.24	2020-04-27T19:55:32.320	0.56
2016-05-14T08:21:54.560	0.16	2019-11-05T06:11:08.600	0.32	2020-04-27T20:01:45.800	0.40
2016-05-14T22:25:21.840	0.04	2019-11-05T07:17:17.880	0.08	2020-04-27T20:13:38.280	0.08
2016-05-16T20:49:47.000	0.04	2020-04-10T09:43:54.280	0.20	2020-04-27T20:14:51.440	0.04
2016-05-18T07:49:34.000	0.20	2020-04-27T18:26:20.160	0.12	2020-04-27T20:15:20.640	1.28
2016-05-18T09:09:23.880	0.20	2020-04-27T18:31:05.800	0.20	2020-04-27T20:17:09.160	0.16
2016-05-18T10:07:26.760	0.04	2020-04-27T18:31:25.240	0.20	2020-04-27T20:17:27.320	0.12
2016-05-18T10:28:02.760	0.16	2020-04-27T18:31:33.800	5.00	2020-04-27T20:17:50.440	0.28
2016-05-18T15:33:47.000	0.08	2020-04-27T18:31:39.240	1.32	2020-04-27T20:17:51.360	0.44
2016-05-18T17:00:31.720	0.04	2020-04-27T18:31:41.080	0.44	2020-04-27T20:17:58.440	0.16
2016-05-18T19:40:37.080	0.60	2020-04-27T18:31:42.120	0.24	2020-04-27T20:19:48.400	0.08
2016-05-19T11:46:52.480	0.12	2020-04-27T18:31:44.640	0.16	2020-04-27T20:19:49.480	0.20
2016-05-19T11:59:32.600	0.08	2020-04-27T18:31:45.520	0.08	2020-04-27T20:21:51.840	0.04
2016-05-19T12:07:46.600	0.12	2020-04-27T18:31:48.360	0.76	2020-04-27T20:21:52.280	0.16
2016-05-19T19:59:54.960	0.32	2020-04-27T18:32:00.520	0.52	2020-04-27T20:21:55.160	0.60
2016-05-20T03:24:12.840	0.04	2020-04-27T18:32:05.840	0.04	2020-04-27T20:25:53.480	0.36
2016-05-20T05:21:33.480	0.16	2020-04-27T18:32:14.680	0.44	2020-04-27T21:14:45.600	0.32
2016-05-20T16:21:43.160	0.12	2020-04-27T18:32:30.680	0.64	2020-04-27T21:15:36.400	0.16
2016-05-20T21:42:29.320	0.28	2020-04-27T18:32:31.520	0.68	2020-04-27T21:20:55.560	0.12
2016-05-21T03:23:36.640	0.12	2020-04-27T18:32:39.000	0.08	2020-04-27T21:43:06.320	0.24
2016-06-07T03:48:59.400	0.04	2020-04-27T18:32:41.640	2.20	2020-04-27T21:48:44.080	0.44
2016-06-18T01:42:55.560	0.08	2020-04-27T18:32:54.480	0.68	2020-04-27T21:59:22.520	0.24
2016-06-18T20:27:25.760	0.12	2020-04-27T18:32:56.240	0.20	2020-04-27T22:47:05.360	0.52
2016-06-20T15:16:34.840	0.28	2020-04-27T18:32:58.320	0.04	2020-04-27T22:55:19.920	0.28
2016-06-22T13:45:23.680	0.16	2020-04-27T18:32:59.680	0.36	2020-04-27T23:02:53.520	0.60
2016-06-23T15:16:09.040	0.12	2020-04-27T18:33:00.840	0.48	2020-04-27T23:06:06.160	0.16
2016-06-23T15:16:26.840	0.20	2020-04-27T18:33:02.240	0.16	2020-04-27T23:25:04.360	0.52
2016-06-23T16:17:04.200	0.08	2020-04-27T18:33:02.720	0.68	2020-04-27T23:27:46.320	0.08
2016-06-23T16:49:57.480	0.12	2020-04-27T18:33:04.560	0.04	2020-04-27T23:44:31.800	0.72
2016-06-23T17:39:22.360	0.08	2020-04-27T18:33:04.640	1.08	2020-04-28T00:19:44.200	0.08
2016-06-23T17:55:48.800	0.08	2020-04-27T18:33:05.840	12.72	2020-04-28T00:23:04.760	0.16
2016-06-23T19:24:40.040	0.08	2020-04-27T18:33:24.320	0.24	2020-04-28T00:24:30.320	0.28
2016-06-23T19:36:27.360	0.20	2020-04-27T18:33:25.480	0.44	2020-04-28T00:37:36.160	0.12
2016-06-23T19:38:00.000	0.12	2020-04-27T18:33:31.760	0.32	2020-04-28T00:39:39.600	0.56
2016-06-23T20:06:37.120	0.16	2020-04-27T18:33:33.000	0.52	2020-04-28T00:41:32.160	0.44
2016-06-25T08:04:52.960	0.08	2020-04-27T18:33:53.120	0.24	2020-04-28T00:43:25.200	0.48
2016-06-26T06:03:14.960	0.32	2020-04-27T18:34:05.720	0.44	2020-04-28T00:44:08.240	0.40
2016-06-26T13:54:30.720	0.84	2020-04-27T18:34:46.040	0.24	2020-04-28T00:44:09.280	0.28
2016-06-26T17:50:03.240	0.04	2020-04-27T18:34:47.240	0.32	2020-04-28T00:45:31.160	0.08
2016-06-26T20:34:49.320	0.08	2020-04-27T18:34:57.400	0.44	2020-04-28T00:46:00.040	0.80
2016-06-27T01:50:15.840	0.08	2020-04-27T18:35:05.320	0.20	2020-04-28T00:46:06.440	0.04
2016-06-27T09:44:07.720	0.04	2020-04-27T18:35:46.640	0.08	2020-04-28T00:46:17.960	0.32

Table 1
(Continued)

Burst Time (UTC)	Duration (s) 8–900 keV	Burst Time (UTC)	Duration (s) 8–900 keV	Burst Time (UTC)	Duration (s) 8–900 keV
2020-04-28T00:46:20.200	0.68	2021-02-11T13:43:16.760	0.08	2021-09-11T15:17:45.280	0.92
2020-04-28T00:46:23.560	0.84	2021-02-16T22:20:39.600	0.36	2021-09-11T15:26:11.560	0.12
2020-04-28T00:46:43.080	0.52	2021-06-24T02:34:10.200	0.08	2021-09-11T15:32:33.400	0.36
2020-04-28T00:47:57.560	0.20	2021-07-06T03:50:09.720	0.24	2021-09-11T15:34:39.960	0.28
2020-04-28T00:48:49.280	0.60	2021-07-06T15:01:52.600	0.24	2021-09-11T15:38:25.680	0.16
2020-04-28T00:49:00.320	0.12	2021-07-07T00:33:31.640	0.16	2021-09-11T16:36:57.840	0.12
2020-04-28T00:49:01.120	0.24	2021-07-07T15:45:11.080	0.20	2021-09-11T16:39:20.920	0.08
2020-04-28T00:49:01.960	0.16	2021-07-07T18:08:16.920	0.08	2021-09-11T16:50:03.840	0.04
2020-04-28T00:49:06.480	0.08	2021-07-08T00:18:18.560	0.32	2021-09-11T17:01:09.760	1.44
2020-04-28T00:49:16.640	0.28	2021-07-08T09:03:41.640	0.08	2021-09-11T17:10:48.600	0.48
2020-04-28T00:49:22.400	0.12	2021-07-15T06:43:16.360	0.12	2021-09-11T18:54:36.040	0.04
2020-04-28T00:49:27.320	0.08	2021-07-15T09:15:18.840	0.12	2021-09-11T20:05:46.200	0.08
2020-04-28T00:49:46.160	0.04	2021-08-05T00:08:56.000	0.20	2021-09-11T20:13:40.480	0.32
2020-04-28T00:49:46.680	0.20	2021-09-06T01:44:30.080	0.16	2021-09-11T20:22:58.800	1.28
2020-04-28T00:50:01.040	0.52	2021-09-09T18:57:14.840	0.12	2021-09-11T22:51:41.560	0.12
2020-04-28T00:50:22.000	0.04	2021-09-09T20:21:28.360	0.08	2021-09-12T00:34:37.320	0.76
2020-04-28T00:51:35.920	0.08	2021-09-10T00:45:46.880	1.44	2021-09-12T00:45:49.400	0.04
2020-04-28T00:51:55.440	0.12	2021-09-10T00:46:21.000	0.08	2021-09-12T05:24:05.640	0.08
2020-04-28T00:52:06.240	0.04	2021-09-10T01:00:43.680	0.80	2021-09-12T07:04:53.840	0.08
2020-04-28T00:54:57.480	0.16	2021-09-10T01:04:33.360	0.48	2021-09-12T07:28:07.240	0.36
2020-04-28T00:56:49.640	0.32	2021-09-10T01:06:23.720	0.64	2021-09-12T10:10:11.680	0.12
2020-04-28T01:04:03.160	0.04	2021-09-10T01:08:40.680	0.56	2021-09-12T12:19:20.440	0.48
2020-04-28T02:00:11.440	0.40	2021-09-10T01:13:17.400	0.04	2021-09-12T13:55:16.440	0.08
2020-04-28T02:27:24.920	0.04	2021-09-10T01:13:57.800	0.04	2021-09-12T15:03:50.600	0.40
2020-04-28T03:32:00.600	0.08	2021-09-10T01:14:36.880	0.32	2021-09-12T16:26:08.040	0.08
2020-04-28T03:47:52.160	0.24	2021-09-10T01:17:19.080	0.16	2021-09-12T20:16:10.400	1.00
2020-04-28T04:09:47.320	0.08	2021-09-10T01:18:54.160	0.60	2021-09-12T20:16:20.280	0.12
2020-04-28T05:56:30.560	0.08	2021-09-10T01:20:48.320	0.08	2021-09-12T20:57:28.720	0.16
2020-04-28T09:51:04.880	0.28	2021-09-10T01:21:49.600	0.08	2021-09-12T20:57:29.320	0.08
2020-04-29T20:47:28.000	0.20	2021-09-10T01:31:40.040	0.48	2021-09-12T23:19:32.080	0.28
2020-05-03T23:25:13.440	0.24	2021-09-10T01:34:18.880	0.16	2021-09-13T00:27:24.920	0.56
2020-05-16T18:12:52.120	0.08	2021-09-10T02:21:06.400	0.16	2021-09-13T03:29:21.440	0.08
2020-05-19T18:32:30.320	0.68	2021-09-10T02:36:38.240	0.56	2021-09-13T04:52:06.520	0.12
2020-05-20T14:10:49.840	0.12	2021-09-10T02:44:34.160	0.08	2021-09-13T08:16:46.760	0.12
2020-05-20T21:47:07.520	0.48	2021-09-10T05:35:55.480	0.12	2021-09-13T19:51:33.160	0.20
2021-01-24T20:48:23.960	0.08	2021-09-10T05:40:48.640	0.08	2021-09-14T06:12:45.200	0.04
2021-01-28T23:35:02.480	0.16	2021-09-10T09:12:48.880	0.08	2021-09-14T11:10:36.200	0.12
2021-01-29T02:46:22.560	0.20	2021-09-10T13:40:20.360	0.24	2021-09-14T14:44:21.240	0.08
2021-01-29T07:00:01.000	0.24	2021-09-10T15:50:56.880	0.08	2021-09-16T17:28:31.040	0.08
2021-01-29T10:35:39.960	0.32	2021-09-10T23:40:34.440	0.32	2021-09-16T20:24:09.120	0.12
2021-01-29T15:23:29.920	0.08	2021-09-11T02:28:08.400	0.08	2021-09-18T10:39:07.040	0.08
2021-01-29T15:29:23.920	0.48	2021-09-11T02:28:11.680	0.08	2021-09-20T05:39:51.480	0.08
2021-01-29T18:38:04.840	0.12	2021-09-11T03:02:38.320	0.08	2021-09-22T01:40:44.280	0.08
2021-01-29T21:15:55.960	0.08	2021-09-11T05:32:38.640	0.28	2021-09-22T09:57:03.320	0.04
2021-01-30T00:41:51.160	0.16	2021-09-11T10:42:51.840	0.08	2021-09-25T03:03:28.320	0.12
2021-01-30T03:24:38.360	0.12	2021-09-11T11:45:04.960	0.04	2021-09-26T15:08:11.880	0.08
2021-01-30T08:39:53.840	0.16	2021-09-11T11:53:57.280	0.08	2021-09-27T19:46:09.760	0.08
2021-01-30T10:35:35.120	0.08	2021-09-11T13:27:33.840	0.08	2021-09-30T01:31:06.160	0.12
2021-01-30T17:40:54.760	0.16	2021-09-11T13:28:54.960	0.20	2021-09-30T20:41:15.800	0.20
2021-01-30T21:01:22.840	0.12	2021-09-11T13:29:08.200	0.04	2021-10-01T00:04:04.320	0.12
2021-02-02T12:54:26.960	0.24	2021-09-11T14:58:38.600	0.04	2021-10-02T06:08:13.080	0.08
2021-02-05T07:13:15.760	0.08	2021-09-11T15:03:00.400	0.20	2021-10-07T17:39:49.320	0.20
2021-02-07T00:35:52.720	0.12	2021-09-11T15:06:43.200	0.44	2021-10-08T15:57:46.400	0.40
2021-02-10T14:15:07.080	0.08	2021-09-11T15:15:25.400	1.20	2021-10-11T11:59:40.800	0.16
2021-02-11T12:28:00.120	0.04	2021-09-11T15:16:25.720	0.08		

April 27, as shown in Figure 5. We also identified two intermediate bursts (IBs) at 2020-04-27T18:32:41.640 (UTC) and 2020-04-27T18:33:05.840 (UTC), which are characterized by their relatively long durations compared to short-duration bursts. No giant flare was found in our results. About 20 hr later, the IB and burst forest was followed by the X-ray burst associated with a fast radio burst, FRB 200428 (the red vertical line in Figure 4).
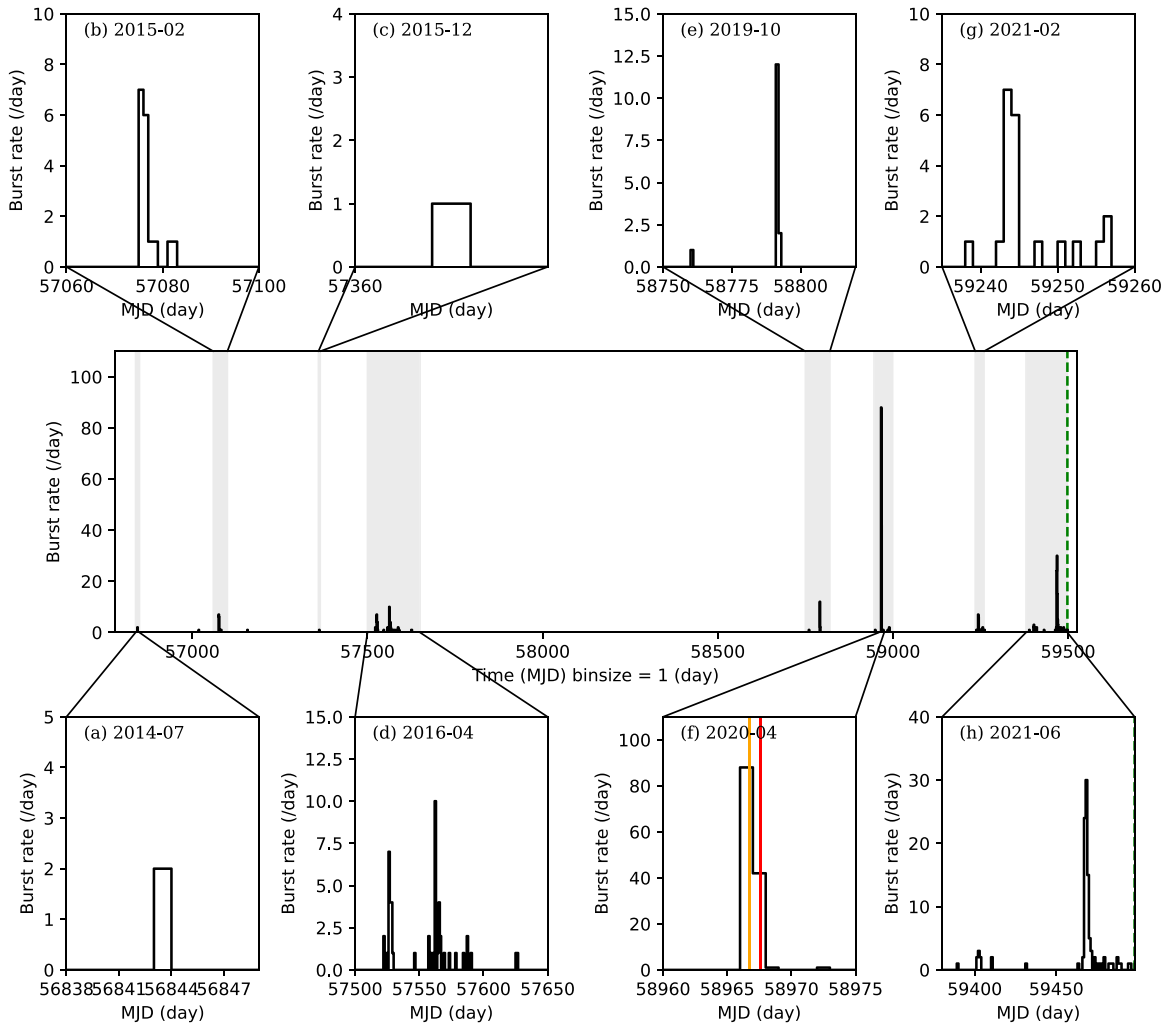
Figure 4. The overall burst rate of our sample from 2014 May 1 to 2021 July 8. The details of the eight bursting phases are shown in the zoomed panels (a, b, c, d, e, f, g, and h). In panel (f), the yellow line represents the burst forest on 2020 April 27. The red line represents the arrival time of SGR-FRB 200428. The dashed green line indicates the last time we checked on the data for this work, which is 2021 October 10.
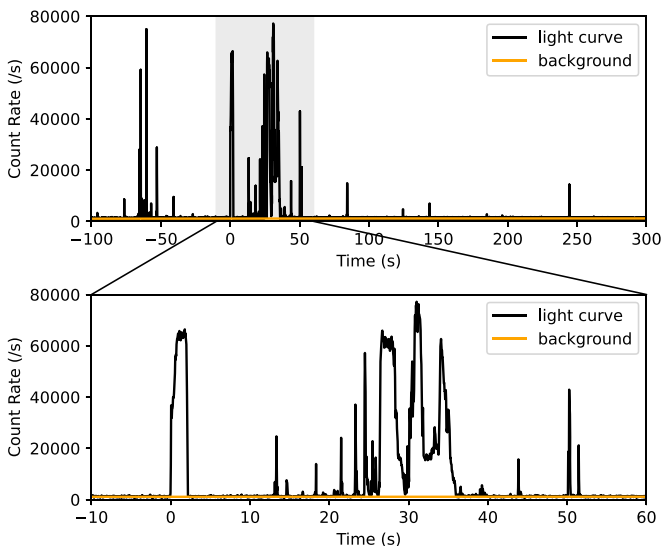

Figure 5. Light curves of the burst forest on 2020 April 27. The yellow curve represents the background. The time corresponding to $T = 0$ is 2020-04-27T18:32:41:650 (UTC).
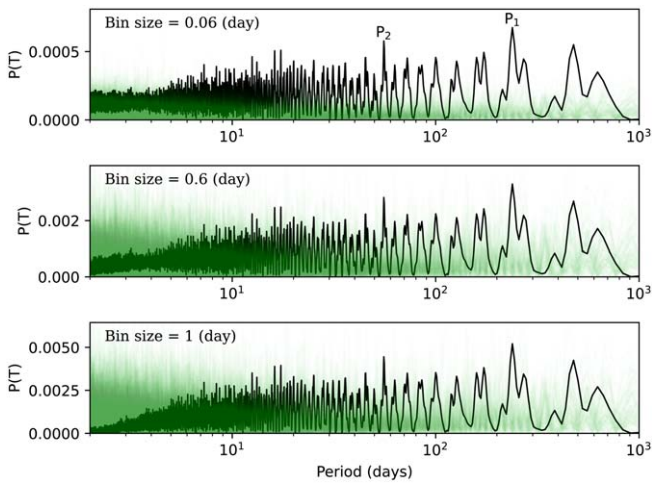
3. Periodicity Analysis

The complete seven-phase, 353-burst events obtained from our data reduction above provide a rich and homogeneous sample to perform the PWB analysis of this magnetar. To do so, we employed the Lomb–Scargle (LS) method,[16] which is a widely used approach to derive the period of unevenly sampled observations (Lomb 1976; Scargle 1982; VanderPlas 2018). To utilize the LS method, one has to bin the observed events into uniform bins and obtain the event rate as a function of time. Based on the various event rate binned with values between 0.06 and 1 day, we calculated their Lomb–Scargle period-ograms of SGR J1935+2154, as shown in Figure 6. The most significant peak in the periodograms is at ∼238 days (P_1), which is roughly consistent with the previous study by Grossan (2021), which proposed a period of about 231 days using a 161-burst sample observed by the IPN network from 2014 to 2020. We noticed that there is one less significant peak presented in Figure 6, namely at ∼55 days (P_2). Both P_1 and P_2 are subject to further significance check before they can be claimed as a period of the SGR.

Figure 6. The Lomb–Scargle periodograms with different bin sizes. There are two significant peaks at period ∼238 days (P_1) and period ∼55 days (P_2). The green lines overplotted in the background represent the periodograms of the 10,000 simulated data sets.
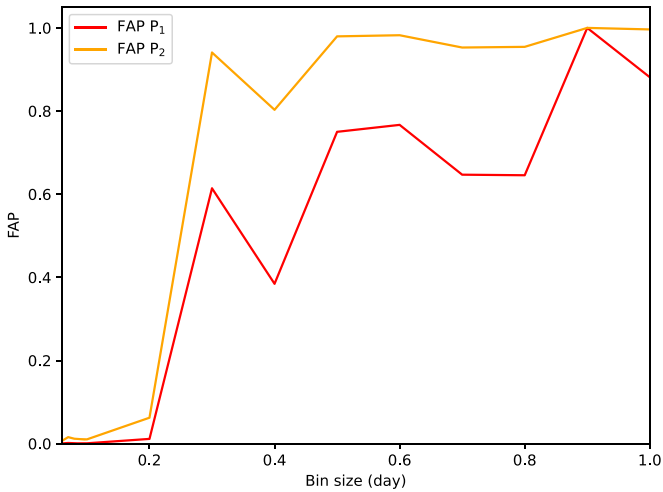

Figure 7. The effect of bin size on FAP. The blue and yellow lines represent the FAPs of P_1 and P_2.

The typical way of quantifying the significance of a peak in a periodogram is the false alarm probability (FAP; Scargle 1982), which measures the probability that a data set with no signal would lead to a peak with a similar magnitude (Vander-Plas 2018). Baluev (2008) derived an analytic FAP based on the theory of extreme values for stochastic processes in the form of

$$FAP(z) = 1 - P_{max}(z, f_{max}), \qquad (1)$$

where z is the height of a peak in periodogram, f_{max} is the maximum frequency of the calculated periodogram, and $P_{max}(z, f_{max})$ denotes the cumulative distribution function of the maximum of z under the null hypothesis in the frequency range between 0 and f_{max}. FAP calculation depends on the size of the input data set, and in our case, the bin size of sampling to obtain the event rate (VanderPlas 2018). To illustrate this, we calculated the FAP values following Equation (1) for the periodograms of the data sets with different bin sizes, as shown in Figure 7 and Table 2. We noticed that the FAP values become stable when the bin size ⩽0.06 day, with typical values of
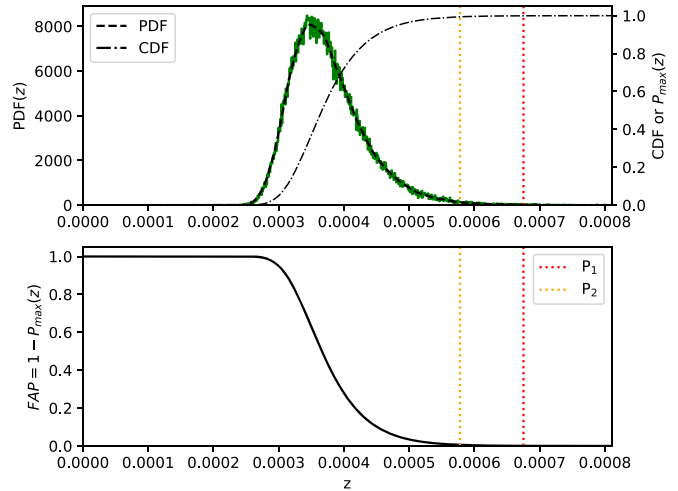

Figure 8. The top panel shows the probability density function (PDF) and cumulative distribution function (CDF) of z (taken under the null hypothesis). The bottom panel shows the FAP curve. The red and yellow dotted lines represent P_1 and P_2. The bin size is 0.06 day.

Table 2
The FAPs with Different Bin Sizes

Bin Size (day)	P_1 FAP	P_2 FAP
0.06	0.00068	0.00591
0.07	0.00194	0.01406
0.08	0.00140	0.01032
0.09	0.00129	0.00982
0.10	0.00124	0.00938
0.20	0.01015	0.06160
0.30	0.61819	0.94697
0.40	0.38717	0.80979
0.50	0.75718	0.98207
0.60	0.77241	0.98597
0.70	0.64913	0.95684
0.80	0.64938	0.95797
0.90	1.00000	1.00000
1.00	0.89046	0.99775

$FAP(P_1) = 7.7 \times 10^{-4}$ and $FAP(P_2) = 7.0 \times 10^{-3}$. Our calculation suggests that a proper sampling bin size (e.g., ⩽0.06 day or ∼5000 s) is crucial to reflect the temporal structure of the events and to claim the significance of the periodic signal.

Alternatively, one can calculate the FAP through a Monte Carlo simulation. To do so, we simulated 100,000 sets of events. In each set, there are 353 bursts randomly distributed from 2013 January to 2021 October. We then calculate the LS periodogram for each set. By measuring the numbers of cases, N, out of the 100,000 simulations, in which one can reproduce the same or higher height z of the peaks (i.e., P_1 and P_2) in the observed data, we can calculate the FAP as $FAP = \frac{N}{100000}$. Our simulations are shown in Figure 8 and yield a result of $FAP(P_1) = 6.8 \times 10^{-4}$ and $FAP(P_2) = 5.9 \times 10^{-3}$, which is consistent with the result obtained by Equation (1). Based on the above calculation, we claim P_1 is a period of SGR 1935+2154 at the 4.5σ confidence level. On the other hand, P_2 is much less significant with a confidence level less than 4σ. Furthermore, as we show below (Section 4) that P_2 becomes unstable when considering the data gaps, and thus can be a false positive.
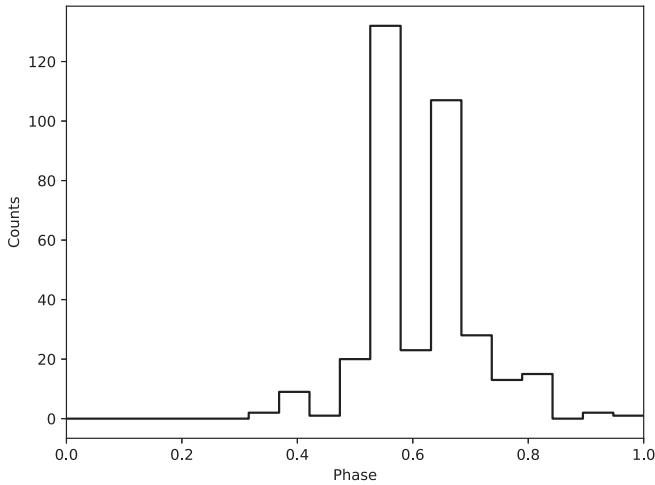
Figure 9. Phase-folded burst rate according to the 238 day period. The duty cycle is determined by the width of the folded data.
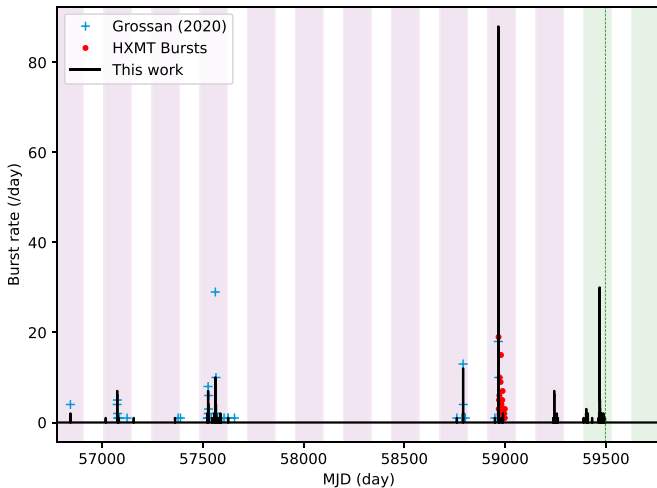

Figure 10. The period plot according to P1. The shaded areas show the active windows, among which the green ones show the predicted two nearest upcoming active windows. Three different samples, this work (black lines), Grossan (2021; blue points), and HXMT bursts (red points) are overplotted with different symbols. The dotted green line indicates the current date, which is 2021 August 10.

Using a period of P_1, we plot the phase-folded event rate in Figure 9, from which we can further calculate a duty cycle to be 63.2%. The active windows from our calculations are marked with pink regions in Figure 10, where we also overplot the Fermi bursts in our sample as well as those IPN bursts from Grossan (2021) and the bursts from the HXMT mission,[17] with the latter two not being taken into account in our fit. One can see that all observed data fully comply with our model's prediction.

4. Implications and Discussions

By analyzing a complete 353-burst sample searched for periodic signal from the 8.5 yr up-to-date continuous event data of Fermi/ GBM mission using the LS methods, we identified a period of 238 days with a 63.2% duty cycle. Our model suggested a total of 12 cycles from 2014 July to date. For such a long time span, the time clustering behavior of the bursts is statistically significant (Denissenya et al. 2021). Our results are fully consistent with all
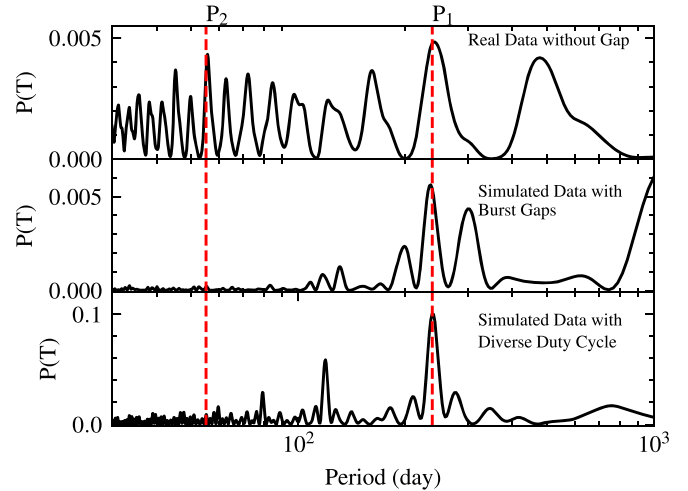
---

[17] http://hxmtweb.ihep.ac.cn/bursts/392.jhtml

Figure 11. The Lomb–Scargle periodogram of the real data without the burst gaps is shown in the top panel. The periodograms of the simulated data are shown in the middle and bottom panels. The dashed vertical red lines mark the two periods. The middle panel is the periodogram of the simulated data with the burst gaps. The bottom panel is the periodogram of the simulated data with different active window widths.

Table 3
The Nearest Upcoming Active Windows Predicted by Our Model

Starting Time (UTC)	Ending Time (UTC)
2021-06-25	2021-11-08
2022-02-19	2022-07-04

the X-ray bursts of SGR J1935+2154 observed by multiple missions to date. Our calculation can predict the next active windows in the nearest future, as listed in Table 3 and overplotted in Figure 10. Interestingly, as of October 10, the current ongoing burst activities of the SGR J1935+2154, which starts from 2021 June 26, are fully within our model-predicted window.

There is a less significant period of $P_2 = 55$ day as presented in Figure 6. We investigate their possible causes through the following analysis:

1. We ignore the burst gaps in 2017 and 2018 and recalculate the Lomb–Scargle periodogram from the real data, as presented in the top panel of Figure 11. Although the peak of P_2 is visible, it becomes much less significant ($<3\sigma$), suggesting that it can be caused by the data gaps.
2. Based on the observed data, a series of points that are distributed with a period of $\sim$238 days and the duty cycle of 63% are simulated. The observation-based burst gaps are then applied to the simulated data. The calculated Lomb–Scargle periodogram is shown in the middle panel of Figure 11. The peak of P_1 persists in this simulation, suggesting that P_1 is not affected by the gap of data.
3. Similar to the above step, but data are simulated with different duty cycles but no data gaps. The peak of P_1 still persists in this simulation, suggesting that it is not affected by the burst active window itself.

Based on our simulation, the period of $P_1 = 238$ days seems to be always stable and reliable. On the other hand, the data gaps of the data may lead to some faked signals which should be studied with caution.

The physical origin of the $P \sim 238$ days, however, remains an open question. Given that there is no evidence showing SGR

J1935+2154 are in a binary system, we focus on the explanations invoking the properties of the magnetar itself. In that regard, the most natural way to cause a period may be the free precession of the magnetar. The NS precession period is derived to be $P_{prec} \sim P_{spin}/\epsilon$ (Levin et al. 2020), where P_{spin} and ϵ are the spin period and the ellipticity of the NS, respectively. By substituting $P_{prec} = 238$ days and $P_{spin} = 3.24$ s (Israel et al. 2016) for SGR J1935+2154, we can derive that $\epsilon \simeq 1.6 \times 10^{-7}$. We can further calculate that the ratio of the poloidal components energy to the total magnetic energy is $\Lambda \simeq 0.83$ (Equation (7) of Mastrano et al. 2013) for simple dipole poloidal-plus-toroidal magnetic field configurations, which suggests that the poloidal component is more dominant than the toroidal component. Interestingly, two FRBs also show periodic behavior. Considering the association between FRB 200428 and the X-ray burst of SGR 1935+2154, their physical origins of periodicity may have a close connection. Therefore, extensive study of the periodicity in X-ray bursts is important to understand the origin of periodic FRBs.

One challenge to our model is that there is no burst observed in 2017 and 2018. Such a gap covers four continuous burst-absent periods. Interestingly, we found that the four periods before and after the gap are both burst-present (Figure 10). This suggests that there may be a superposed $8 \times P \sim 1904$ day period. Such a larger period may be related to the globally evolving collimation of the emission region of SGR J1935+2154. We note that this hypothesis can be tested by checking the (non)presence of bursts in our model-predicted window starting in 2022 February (Table 3).

Our model can also back-predict the active windows. The nearest predicted active window before the first discovery of SGR J1935+2154 is between 2013 September and 2014 January, or between 2009 January and 2009 May if considering the superposed $8 \times P$ period. Both of them are covered by the IPN network and Fermi. However, neither the IPN list (Confirmed SGR Burst & Possible SGR Bursts; http://www.ssl.berkeley.edu/ipn3/masterli.html; Hurley et al. 2009) nor our search has yielded any burst in those windows, even though IPN has operated largely continuously since the year 1990. The nondetection of SGR J1935 +2154 in pre-discovery data suggests that SGR J1935+2154 likely began its active phase around 2014 July.

Software: numpy; matplotlib; pandas; scipy; astropy; baseline[18]; sigma_clip[19]; bayesian_blocks[20]; gbm_drm_gen[21] cartopy[22]; lomb-scargle[23]; pymultinest[24];

---

[18] https://www.rdocumentation.org/packages/baseline/versions/1.3-1
[19] https://docs.astropy.org/en/stable/api/astropy.stats.sigma_clip.html
[20] https://docs.astropy.org/en/stable/api/astropy.stats.bayesian_blocks.html#astropy.stats.bayesian_blocks
[21] https://github.com/grburgess/gbm_drm_gen
[22] https://scitools.org.uk/cartopy/docs/latest/
[23] https://docs.astropy.org/en/stable/timeseries/lombscargle.html
[24] https://github.com/JohannesBuchner/PyMultiNest

ORCID iDs

Jin-Hang Zou ⓘ https://orcid.org/0000-0003-4011-2608
Bin-Bin Zhang ⓘ https://orcid.org/0000-0003-4111-5958
Guo-Qiang Zhang ⓘ https://orcid.org/0000-0001-6545-4802
Yu-Han Yang ⓘ https://orcid.org/0000-0003-0691-6688
Lang Shao ⓘ https://orcid.org/0000-0001-8876-2357
Fa-Yin Wang ⓘ https://orcid.org/0000-0003-4157-7714

References

Baluev, R. V. 2008, MNRAS, 385, 1279
Banas, K. R., Hughes, J. P., Bronfman, L., & Nyman, L. Å. 1997, ApJ, 480, 607
Beloborodov, A. M. 2017, ApJL, 843, L26
Beniamini, P., Wadiasingh, Z., & Metzger, B. D. 2020, MNRAS, 496, 3390
Bochenek, C. D., Ravi, V., Belov, K. V., et al. 2020, Natur, 587, 59
Boggs, S., Hurley, K., Smith, D. M., et al. 2005, GCN, 2936, 1
Burgess, J. M., Yu, H.-F., Greiner, J., & Mortlock, D. J. 2018, MNRAS, 476, 1427
Burns, E., Svinkin, D., Hurley, K., et al. 2021, ApJL, 907, L28
Cameron, P. B., Chandra, P., Ray, A., et al. 2005, Natur, 434, 1112
Cheng, Y., Zhang, G. Q., & Wang, F. Y. 2020, MNRAS, 491, 1498
CHIME/FRB Collaboration, Amiri, M., Andersen, B. C., et al. 2020b, Natur, 582, 351
CHIME/FRB Collaboration, Andersen, B. C., Bandura, K. M., et al. 2020a, Natur, 587, 54
Connaughton, V., Briggs, M. S., Goldstein, A., et al. 2015, ApJS, 216, 32
Cordes, J. M., & Chatterjee, S. 2019, ARA&A, 57, 417
Cruces, M., Spitler, L. G., Scholz, P., et al. 2021, MNRAS, 500, 448
Dai, Z. G., Wang, J. S., Wu, X. F., & Huang, Y. F. 2016, ApJ, 829, 27
Dai, Z. G., & Zhong, S. Q. 2020, ApJL, 895, L1
Denissenya, M., Grossan, B., & Linder, E. V. 2021, PhRvD, 104, 023007
Duncan, R. C., & Thompson, C. 1992, ApJL, 392, L9
Eilers, P. H. 2003, AnaCh, 75, 3631
Feroci, M., Mereghetti, S., Woods, P., et al. 2003, ApJ, 596, 470
Frail, D. A., Kulkarni, S. R., & Bloom, J. S. 1999, Natur, 398, 127
Frederiks, D. D., Palshin, V. D., Aptekar, R. L., et al. 2007, AstL, 33, 19
Fuchs, Y., Mirabel, F., Chaty, S., et al. 1999, A&A, 350, 891
Geng, J. J., & Huang, Y. F. 2015, ApJ, 809, 24
Golenetskii, S. V., Ilinskii, V. N., & Mazets, E. P. 1984, Natur, 307, 41
Grossan, B. 2021, PASP, 133, 074202
Guidorzi, C., Frontera, F., Montanari, E., et al. 2004, A&A, 416, 297
Hurley, K., Cline, T., Mazets, E., et al. 1999, Natur, 397, 41
Hurley, K., Cline, T., Mitrofanov, I. G., et al. 2009, in AIP Conf. Ser. 1133, Gamma-ray Burst: Sixth Huntsville Symp., ed. C. Meegan, C. Kouveliotou, & N. Gehrels (Melville, NY: AIP), 55
Ioka, K., & Zhang, B. 2020, ApJL, 893, L26
Israel, G. L., Esposito, P., Rea, N., et al. 2016, MNRAS, 457, 3448
Katz, J. I. 2016, ApJ, 826, 226
Kouveliotou, C., Dieters, S., Strohmayer, T., et al. 1998b, Natur, 393, 235
Kouveliotou, C., Fishman, G. J., Meegan, C. A., et al. 1993, Natur, 362, 728
Kouveliotou, C., Kippen, M., Woods, P., et al. 1998a, IAU Circ., 6944, 2
Kulkarni, S. R., Ofek, E. O., Neill, J. D., Zheng, Z., & Juric, M. 2014, ApJ, 797, 70
Levin, Y., Beloborodov, A. M., & Bransgrove, A. 2020, ApJL, 895, L30
Li, C. K., Lin, L., Xiong, S. L., et al. 2021, NatAs, 5, 378
Lin, L., Göğüş, E., Roberts, O. J., et al. 2020a, ApJL, 902, L43
Lin, L., Göğüş, E., Roberts, O. J., et al. 2020b, ApJ, 893, 156
Lin, L., Zhang, C. F., Wang, P., et al. 2020c, Natur, 587, 63
Lomb, N. R. 1976, Ap&SS, 39, 447
Lorimer, D. R., Bailes, M., McLaughlin, M. A., Narkevic, D. J., & Crawford, F. 2007, Sci, 318, 777
Lyubarsky, Y. 2014, MNRAS, 442, L9
Lyutikov, M., Barkov, M. V., & Giannios, D. 2020, ApJL, 893, L39
Mastrano, A., Lasky, P. D., & Melatos, A. 2013, MNRAS, 434, 1658
Mazets, E. P., Aptekar, R. L., Cline, T. L., et al. 2008, ApJ, 680, 545
Mazets, E. P., & Golenetskii, S. V. 1981, Ap&SS, 75, 47
Mazets, E. P., Golenetskij, S. V., & Guryan, Y. A. 1979a, SvAL, 5, 343
Mazets, E. P., Golentskii, S. V., Ilinskii, V. N., Aptekar, R. L., & Guryan, I. A. 1979b, Natur, 282, 587
Mazets, E. P., Golenetskii, S. V., Ilinskii, V. N., et al. 1979c, SvAL, 5, 163
Meegan, C., Lichti, G., Bhat, P. N., et al. 2009, ApJ, 702, 791
Mereghetti, S., Savchenko, V., Ferrigno, C., et al. 2020, ApJL, 898, L29
Metzger, B. D., Berger, E., & Margalit, B. 2017, ApJ, 841, 14

Ofek, E. O., Kulkarni, S. R., Nakar, E., et al. 2006, ApJ, 652, 507
Ofek, E. O., Muno, M., Quimby, R., et al. 2008, ApJ, 681, 1464
Olausen, S. A., & Kaspi, V. M. 2014, ApJS, 212, 6
Paczynski, B. 1992, AcA, 42, 145
Petroff, E., Hessels, J. W. T., & Lorimer, D. R. 2019, A&ARv, 27, 4
Platts, E., Weltman, A., Walters, A., et al. 2019, PhR, 821, 1
Rajwade, K. M., Mickaliger, M. B., Stappers, B. W., et al. 2020, MNRAS, 495, 3551
Ridnaia, A., Svinkin, D., Frederiks, D., et al. 2021, NatAs, 5, 372
Scargle, J. D. 1982, ApJ, 263, 835
Scargle, J. D., Norris, J. P., Jackson, B., & Chiang, J. 2013, ApJ, 764, 167
Sridhar, N., Metzger, B. D., Beniamini, P., et al. 2021, ApJ, 917, 13
Stamatikos, M., Malesani, D., Page, K. L., & Sakamoto, T. 2014, GCN, 16520, 1
Svinkin, D., Frederiks, D., Hurley, K., et al. 2021, Natur, 589, 211
Tavani, M., Ursi, A., Verrecchia, F., et al. 2020, ATel, 13686, 1
Thompson, C., & Duncan, R. C. 1995, MNRAS, 275, 255
Thompson, C., & Duncan, R. C. 1996, ApJ, 473, 322
van Kerkwijk, M. H., Kulkarni, S. R., Matthews, K., & Neugebauer, G. 1995, ApJL, 444, L33
VanderPlas, J. T. 2018, ApJS, 236, 16

Vianello, G. 2018, ApJS, 236, 17
Vrba, F. J., Henden, A. A., Luginbuhl, C. B., et al. 2000, ApJL, 533, L17
Wadiasingh, Z., & Timokhin, A. 2019, ApJ, 879, 4
Wang, F. Y., & Yu, H. 2017, Journal of Cosmology and Astro-Particle Physics, 2017, 023
Whittaker, E. T. 1922, in Proc. of the Edinburgh Mathematical Society, 41 (Cambridge: Cambridge Univ. Press) , 63
Woods, P. M., Kouveliotou, C., Göğüş, E., et al. 2001, ApJ, 552, 748
Woods, P. M., Kouveliotou, C., van Paradijs, J., et al. 1999, ApJL, 519, L139
Woods, P. M., & Thompson, C. 2006, in Compact Stellar X-ray Sources, ed. W. Lewin & M. Van der Klis, Vol. 39 (Cambridge: Cambridge Univ. Press), 547
Xiao, D., Wang, F., & Dai, Z. 2020, SCPMA, 64, 249501
Yang, J., Chand, V., Zhang, B.-B., et al. 2020, ApJ, 899, 106
Yang, Y.-H., Zhang, B.-B., Lin, L., et al. 2021, ApJL, 906, L12
Younes, G., Güver, T., Kouveliotou, C., et al. 2020, ApJL, 904, L21
Younes, G., Kouveliotou, C., Jaodand, A., et al. 2017, ApJ, 847, 85
Zanazzi, J. J., & Lai, D. 2020, ApJL, 892, L15
Zhang, B. 2020, Natur, 587, 45
Zhang, G. Q., Tu, Z.-L., & Wang, F. Y. 2021, ApJ, 909, 83